








Generalized and Mechanistic PV Module Performance Prediction From Computer Vision and Machine Learning on Electroluminescence Images

Ahmad Maroof Karimi , Justin S. Fada , Nicholas A. Parrilla , Benjamin G. Pierce , Mehmet Koyutürk , Roger H. French , *Member, IEEE*, and Jennifer L. Braid , *Member, IEEE*

Abstract—Electroluminescence (EL) imaging of photovoltaic (PV) modules offers high-speed, high-resolution information about device performance, affording opportunities for greater insight and efficiency in module characterization across manufacturing, research and development, and power plant operations and management. Predicting module electrical properties from EL image features is a critical step toward these applications. In this article, we demonstrate quantification of both generalized and performance mechanism-specific EL image features, using pixel intensity-based and machine learning classification algorithms. From EL image features, we build predictive models for PV module power and series resistance, using time-series current–voltage (I – V) and EL data obtained stepwise on five brands of modules spanning three Si cell types through two accelerated exposures: damp heat (DH) (85 °C/85% RH) and thermal cycling (TC) (IEC 61215). In total, 195 pairs of EL images and I – V characteristics were analyzed, yielding 11 700 individual PV cell images. A convolutional neural network was built to classify cells by the severity of busbar corrosion with high accuracy (95%). Generalized power predictive models estimated the maximum power of PV modules from EL images with high confidence and an adjusted- R^2 of 0.88, across all module brands and cell types in extended DH and TC exposures. Mechanistic degradation prediction was demonstrated by quantification of busbar corrosion in EL images of three module brands

in DH, and subsequent modeling of series resistance using these mechanism-specific EL image features. For modules exhibiting busbar corrosion, we demonstrated series resistance predictive models with adjusted- R^2 of up to 0.73.

Index Terms—Computer vision, convolutional neural network (CNN), corrosion, damp heat (DH), electroluminescence (EL) imaging, thermal cycling (TC), photovoltaic (PV) module degradation.

I. INTRODUCTION

WHILE module-level current–voltage (I – V) features relate to particular module degradation or performance phenomena [1]–[4], these quantities yield only a coarse measure of performance in heterogeneous systems as they measure a single electrical signal for the full module, which consists of 60, 72, or 96 full-size photovoltaic (PV) cells. For example, decreasing short-circuit current (I_{sc}) and shunt resistance (R_{sh}) are sometimes related to cracked cells [5], and increasing series resistance (R_s) can be related to corrosion of cell metallization or interconnects. However, the specific module components and degradation mechanisms leading to power loss cannot be determined from I – V features alone.

Visual inspection of test modules can give additional insights into their performance and degradation behaviors, however, these are typically only qualitative and observational in nature. High-density quantitative data that provides information on cell variability and module component degradation can be obtained using image-based measurements such as standard white-light photography, electroluminescence (EL), photoluminescence, ultraviolet (UV) fluorescence, and IR thermography.

EL imaging uses an applied forward-bias voltage across the semiconductor junction to cause radiative charge carrier recombination, with photons emitted in the near-infrared spectral range for silicon. Each pixel represents a spatially resolvable data point of local photon emission registered on the camera sensor, typically generating millions of data points in each module image [1], [6]. Hence, EL images are rich in spatial information related to module performance and condition including cracking, shunting, corrosion, and other degradation mechanisms [7], [8]. Digital EL images can be algorithmically processed to extract features pertaining to overall module performance and specific degradation mechanisms both at the module level and at the cell level by slicing apart the module image after processing.

Manuscript received October 17, 2019; revised December 11, 2019 and January 24, 2020; accepted February 3, 2020. This work was supported by the U.S. Department of Energy's Office of Energy Efficiency and Renewable Energy (EERE) under Solar Energy Technologies Office (SETO) Agreement no. DE-EE-0008172. The work of Jennifer L. Braid was supported by the U.S. Department of Energy (DOE) Office of Energy Efficiency and Renewable Energy administered by the Oak Ridge Institute for Science and Education (ORISE) for the DOE. ORISE is managed by Oak Ridge Associated Universities (ORAU) under DOE Contract no. DE-SC0014664. (*Corresponding author: Jennifer Braid.*)

Ahmad Maroof Karimi and Benjamin G. Pierce are with SDLE Research Center, Case Western Reserve University, Cleveland, OH 44106 USA, and also with the Department of Computer and Data Sciences, Case Western Reserve University, Cleveland, OH 44106 USA (e-mail: axk962@case.edu; bgp12@case.edu).

Justin S. Fada and Nicholas A. Parrilla are with SDLE Research Center, Case Western Reserve University, Cleveland, OH 44106 USA (e-mail: jsf77@case.edu; nap65@case.edu).

Mehmet Koyutürk is with the Department of Computer and Data Sciences, Case Western Reserve University, Cleveland, OH 44106 USA (e-mail: mxk331@case.edu).

Roger H. French and Jennifer L. Braid are with SDLE Research Center, Case Western Reserve University, Cleveland, OH 44106 USA, and also with the Department of Materials Science and Engineering, Case Western Reserve University, Cleveland, OH 44106 USA (e-mail: roger.french@case.edu; jlb269@case.edu).

Color versions of one or more of the figures in this article are available online at <http://ieeexplore.ieee.org>.

Digital Object Identifier 10.1109/JPHOTOV.2020.2973448

In our prior work, we demonstrated an automated image processing pipeline for standardizing module-level EL images and extracting cell-level images, correlation of EL and $I-V$ features, machine learning classification of degraded cell EL images, and $I-V$ feature extraction method from $I-V$ curves [9]–[13]. Some researchers have used cell-level image features to study spatial and cell variations in module performance [8], [14]–[19].

Our goal is to predict module-level power output and mechanistic degradation from EL image features derived with algorithmic and machine learning techniques. Prediction of cell and module performance with an imaging technique such as EL would enable high-speed characterization of modules both on the manufacturing line and as fielded outdoors. Here, we introduce automated methods for calculating various pixel intensity-based EL image features. Then, we use a convolutional neural network (CNN) to classify cell-level images by their level of corrosion, and calculate a module-level corrosion metric based on the cell classes. Finally, we build polynomial regression models to predict P_{mp} and R_s from the algorithmic and machine learning-derived EL image features and report the accuracy of each approach. Pixel intensity-based EL image features including the median pixel intensity and fraction of dark pixels yield the best-generalized power prediction models across five brands of PV modules in two exposure types, with adjusted- R^2 of 0.88 and 0.87, respectively. We also demonstrate degradation mechanism-specific prediction of series resistance from EL image quantification of gridline corrosion.

In this article, we use the terms “feature” or “variable” to describe the quantitative characteristics derived from EL images or $I-V$ curves, so as not to be confused with “parameters,” which are learned by the machine during training of the CNN, or describe statistical models relating the variables.

II. EXPERIMENTAL METHODS

The dataset used in this article consists of $I-V$ curves and EL images taken on 3 samples each of 5 brands (labeled A through E) in 2 accelerated exposures types for a total of 30 commercial 60-cell modules. These modules span three silicon PV cell types: mono-crystalline aluminum back surface field (Al-BSF), multicrystalline Al-BSF, and mono-crystalline passivated emitter and rear contact cell. The modules were exposed to standard IEC 61215 damp-heat (DH) (85 °C/85% RH) or thermal cycle test conditions [20], with $I-V$ curves and EL images captured at set step wise exposure intervals. For DH, 15 modules were measured at 500 h intervals from 0 to 3000 h, and 4 modules continued exposure up to 4200 h with measurements at 300-h intervals. For thermal cycling (TC), 15 modules were measured at 200 cycle intervals from 0 to 600 cycles, and 4 modules continued exposure up to 1000 cycles with measurements at 100 cycle intervals. $I-V$ curves were obtained with a Spire 4600SLP flash solar simulator. EL images were captured at module I_{sc} with a Sensovation coolSamBa HR-830 8.3 megapixel camera [21]. A subset of the dataset containing EL cell images of one brand having three samples exposed under DH condition is shared online¹ [22].

III. ANALYTICAL METHODS: IMAGE PROCESSING AND FEATURE EXTRACTION

The process by which EL images are captured leads to variation in module orientation between images. To ensure the images are uniformly oriented and registered for analysis, we created an image processing pipeline, which has been discussed in our previous work [9], [11], [12]. Filtering and thresholding methods are used to initially preprocess the data to remove barrel distortion, reduce noise, and remove unimportant background data. With a noise-reduced image, a convex hull algorithm is used to identify cell areas and mark them as a “1” (white pixel) while every other pixel is assigned a “0” (black pixel). A series of 1-D x -axis and y -axis parallel slices are taken through the binary array to identify the steps up (0 to 1) and steps down (1 to 0) across the slice. These steps correspond to the module edge. A regression model is fit to the points along the module edge, and the intersections of the edge lines identify the corners of the PV module. A perspective transformation is, then, applied to uniformly orient and planarize the module image resulting in the final planar-indexed module image ready for subsequent analysis. We have published this EL image processing pipeline as a Python package called *pimage*² [23].

After processing, each module EL image is 8-bit and 2500×1500 pixels, or 3 750 000 individual data points existing as light intensities values between 0 (black) and 255 (white). Then, we segment module images into 60 cell-level images and resize each of them to a resolution 250×250 pixels. The 30 modules evaluated stepwise through DH and TC exposures yielded 195 module-level EL images, from which 11 700 cell-level images were extracted. The extracted cell images were, then, used to calculate the following features: 1) median intensity (F_{med}), 2) fraction of dark pixels (F_{FDP}), 3) normalized busbar width (F_{NBBW}), and 4) busbar corrosion ratio F_{BBCR} . Algorithmic determination of these four module-level EL features are described in the following sections.

A. Median Intensity

Pixel intensity in an EL image corresponds to the spatial electrical activity of the PV module, and, therefore, its ability to generate power. Unlike averaging, median intensity (F_{med}) removes the effects of outliers, and, therefore, is more representative of the overall performance. Here, we calculated the median intensity for each cell-level image, and, then, calculated the median of all the median intensities of the cells for each module-level image to obtain a module-level median intensity.

B. Fraction of Dark Pixels

The fraction of dark pixels (F_{FDP}) corresponds to the area of a cell that emits fewer photons compared with the rest of the cell, i.e., the less active or inactive cell area. In other words, F_{FDP} corresponds to the region, which generates less electricity when light is incident on the cell. F_{FDP} is computed for each cell of a module and, then, the average value of all cells in a module gives F_{FDP} of the module. F_{FDP} is calculated by splitting the density plot (see Fig. 2) of pixel values into two bins by the midpoint

¹[Online]. Available: <https://osf.io/8zkqg/>

²[Online]. Available: <https://pypi.org/project/pimage/>



Fig. 1. Example raw EL image from DH exposure, exhibiting out of plane tilt and barrel distortion.

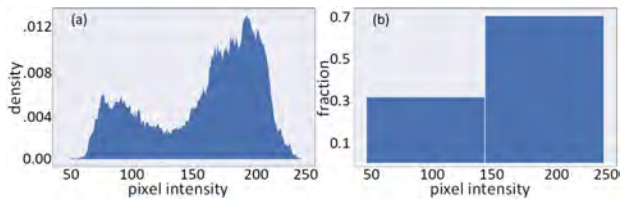


Fig. 2. Example pixel intensity plot for cell-level EL image: (a) probability density plot, (b) probability density plot converted to dark and bright bins.

value, and, then, dividing the number of pixels in the lower bin by the total number of pixels.

C. Normalized Busbar Width

The normalized busbar width (F_{NBW}) is calculated to quantify the extent of busbar corrosion. Front side cell corrosion often manifests in EL images as darkening of the region near the busbar [see Fig. 3(a)]. F_{NBW} is calculated using a peak detection strategy to measure the width of the darkened areas [24].

After the cell is extracted from the module images, the average pixel intensity value in the matrix row parallel to the busbar direction is calculated. This is done for every row of the image matrix leading to 250 data points in the case of our 250×250 pixel cell images. A plot representing these values can be seen in Fig. 3(b) for the cell image in Fig. 3(a). To determine the width of the dark area around the busbar, the center of each busbar is first located by using a minimization peak finding scheme. Depending on the cell geometry, this results in 3 or 4 points corresponding to the busbar centers. Starting from those center busbar points, an algorithm begins moving to the left and right until the slope nears zero. The distance between these points is the characteristic busbar width. However, since a single value is desired for each cell image, the busbar widths for a particular cell are averaged and, then, normalized by the side length of the cell image, as represented by

$$F_{\text{NBW}} = \frac{\sum_{i=1}^N W_i}{N \times L} \quad (1)$$

where N is the number of busbars, W_i is the i th busbar width in pixels, and L is the side dimension of the cell image in pixels. F_{NBW} was calculated for all cells in module brands A, B, and D through DH exposure (brands C and E were omitted because of exhibiting different degradation patterns).

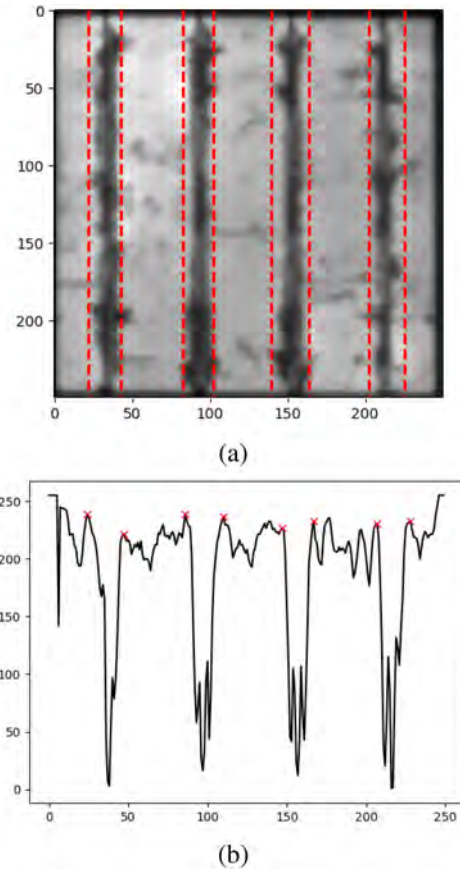


Fig. 3. Normalized busbar width example. (a) Representative cell image with busbar darkening. (b) Average intensity values for each column of the cell image parallel to the busbars. The four smallest minima indicating the busbar centers have a red "X" on each side indicating the point where the slope of the column average intensity goes to zero, corresponding to the edge of the darkened area. [24]

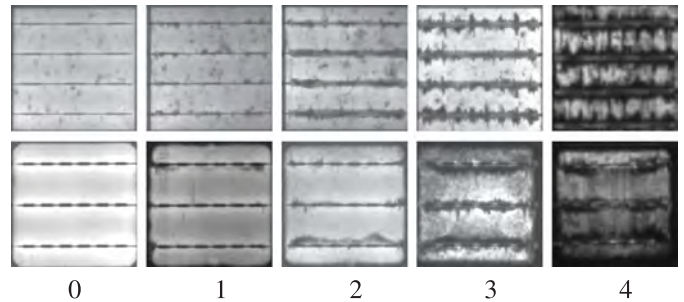


Fig. 4. Examples of cells labeled into five levels of busbar darkening ranging from 0 to 4, such that 0 exhibits no busbar corrosion, and 4 is most severely corroded.

D. Busbar Corrosion Ratio

The busbar corrosion ratio (F_{BCR}) is a module-level attribute that quantifies the overall busbar corrosion in a module from its cell-level images. In this method, we first label cells into different levels of corrosion ranging from 0 to 4, as shown in Fig. 4. This classification process is performed by supervised machine learning with a CNN.

The CNN method is one of the most popular algorithms for classification of images [25]–[29]. We demonstrated in our

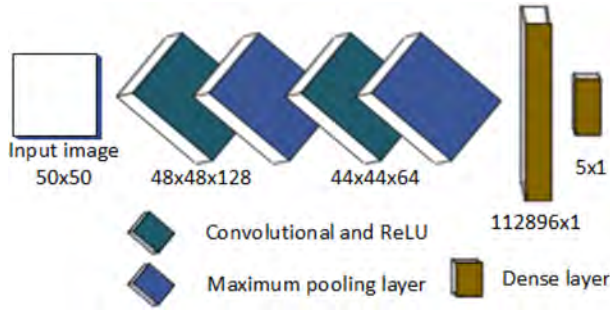


Fig. 5. Architecture of the CNN used for the classification of busbar corrosion levels. Cell-level images are reduced to 50×50 pixel resolution for input, and the output layer is a 5-valued vector indicating the cell corrosion classification.

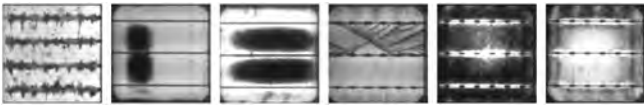


Fig. 6. EL images of cells demonstrating diversity in degradation signatures at various steps of DH or TC within our dataset.

earlier work that CNN was the best classifier to detect different degradation types in EL images of PV cells [12].

Cell-level EL images from brands exhibiting busbar corrosion (brands A, B, and D) in DH exposure were first classified manually into five levels of corrosion (0 to 4) as shown in Fig. 4. We changed the size of images from 250×250 to 50×50 pixels because classification model performed better for images of size 50×50 pixels.

The layer structure of the CNN classifier is shown in Fig. 5. The first layer is an input layer for cell images of size 50×50 , and the next four layers are alternating convolutional and maximum pooling layers. The kernel size in both layer types is 3×3 and the stride in the maximum pooling layer is (1,1). The activation function deployed in the model is rectified linear unit, which is $\max(0, x)$ and applied on each element of convolutional layer. The CNN was implemented in TensorFlow [30] using Keras [31] and Python [32], and run on GPU. We divided the dataset into training, validation, and testing sets, with 65%, 15%, and 20% of datapoints, respectively. The training data were used for model training, the validation set was used for tuning model hyperparameters, and the testing set was used for assessing model performance. We augmented the training set by flipping the images across X- and Y-axes, and rotating 180° as described in [12].

The $F_{\text{BB CR}}$ is the average corrosion classification value assigned by the CNN for all cell-level images from a given module-level image. Therefore, the $F_{\text{BB CR}}$ is a real number in the range of 0–4.

It is to be noted that F_{NBBW} , and $F_{\text{BB CR}}$ are calculated only for brands (A, B, and D) exhibiting busbar corrosion as shown by sample cell images in Fig. 4, whereas F_{med} and F_{FDP} are calculated for all brands exhibiting generalized degradation including busbar corrosion as shown by exemplary images in Fig. 6.

IV. RESULTS

A. Supervised Machine Learning Classification

To calculate $F_{\text{BB CR}}$, we build a CNN model that classifies cell-level images by the severity of busbar corrosion, and the average value of cell classes in a module gives the $F_{\text{BB CR}}$. Cells segmented from the module images of the three module brands that exhibit busbar corrosion in DH exposure were classified into five corrosion levels 0–4, 0 being uncorroded/good cell class and four being the most corroded class as shown in Fig. 4. Total number of cells that were extracted from the module images and successfully labeled into either of the five busbar corrosion classes sum to 4441 images. Out of these, we used 2841 for training the model, 711 images for model validation and hyperparameter tuning, and the remaining 889 cells were used for the test set and to verify the performance of the CNN model on unseen data. The result of the CNN model is shown in Table III. High numbers in the diagonal positions of the matrix indicate that the model has correctly classified a large portion of cell images. The overall accuracy of the model for classification of the testing data (889 cell images) is 95%.

B. Correlation of EL and $I-V$ Features

Here, we explore the correlations between $I-V$ features (V_{oc} , R_{sh} , I_{sc} , P_{mp} , I_{mp} , V_{mp} , FF , and R_s) and the EL features (F_{med} , F_{NBBW} , F_{FDP} , and $F_{\text{BB CR}}$) derived from all module data through DH and TC exposure. Fig. 7 is a pair-wise Pearson linear correlation plot of these variables, with the rightmost two columns containing data from only the three brands in DH exposure, which exhibited busbar darkening in EL images (as opposed to other corrosion signatures such as framing, between busbar darkening, and overall cell darkening). The variables in the heatmap are grouped such that the variables with high correlation coefficients are placed alongside each other. It can be observed that the four EL features are highly correlated with some of the $I-V$ features like R_s , FF , V_{mp} , I_{mp} , and P_{mp} . The high correlation between EL and $I-V$ features suggests that $I-V$ features can be estimated from the EL features using statistical models. Therefore, we further investigate the relationships between two $I-V$ features (R_s and P_{mp}) with our algorithmically derived EL image features. We choose R_s as an electrical signature of corrosion, which is widely accepted as the main mechanism of degradation in DH exposure of PV modules. We also choose P_{mp} to demonstrate generalized prediction of module performance from EL image features.

C. Series Resistance Prediction From EL Image Features

Module-level series resistance is a composite measure of the series resistances of all cells, metallization, and interconnects including the junction box and external leads. As cell defects appear, the module EL pixel intensity distribution becomes more heterogeneous. For example, corrosion of cell metallization leads to darkened cell areas where carrier injection is reduced during dc biasing of the module. As a result, F_{NBBW} , F_{FDP} , and $F_{\text{BB CR}}$ show a positive correlation with R_s , while F_{med} shows negative correlation with R_s as the module degrades, as seen in

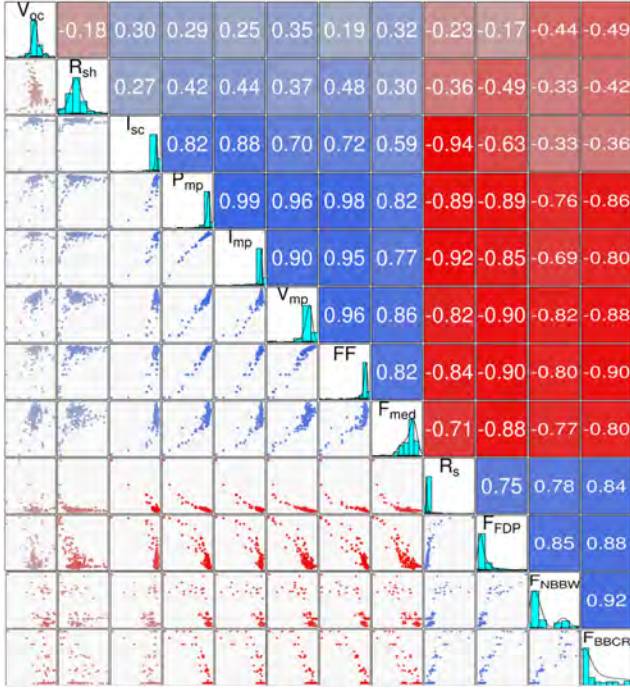


Fig. 7. Pair-wise Pearson correlation heatmap of eight $I-V$ features (V_{oc} , R_{sh} , I_{sc} , P_{mp} , I_{mp} , V_{mp} , FF , and R_s) and four EL features (F_{med} , F_{NBBW} , F_{FDP} , and F_{BBCR}) extracted from stepwise data collected through DH and TC exposures. The Pearson correlation values are color-coded from 1 (blue) for positive correlation to -1 (red) for negative correlation. The Pearson correlation coefficients of F_{NBBW} and F_{BBCR} are derived only from DH exposure data of brands A, B, and D, whereas data from all five brands in both exposures was used for the remaining ten variables.

the pair-wise Pearson correlation heatmap in Fig. 7. The correlation values between R_s and F_{med} , F_{NBBW} , F_{FDP} , and F_{BBCR} are -0.71 , 0.78 , 0.75 , and 0.84 , respectively, consistent with the high correlation among the EL image features themselves.

In both DH and TC, the overall EL image brightness decreases as a function of exposure duration, while R_s increases as corrosion develops. The plots in Fig. 8 are shown for normalized values of features; solid lines in the plots represents normalized series resistance (R_{s-n}), whereas dashed lines represent normalized EL features (represented with $' - n'$ as a suffix in subscript). All normalization is performed relative to the initial value of $I-V$ or EL image feature. Curves are color-coded according to the five brands, and each module has a corresponding pair of solid and dashed curves. Average values of correlation shown between R_s and the image feature are calculated first applying Fisher's Z transformation on the correlation coefficients and, then, taking the mean of the Fisher's Z transform values and converting the mean back to a correlation coefficient [33]. We observe that the dashed and solid lines of the same color show similar trends conforming to our expectation that an EL image feature and R_s correlate for a module as it degrades. Curves in the plots are fitted using "Loess," a nonparametric regression method [34]. An advantage of using the Loess is that it does not require *a priori* functional form of the curve and uses least-square local regression with a sliding window size of 0.75. The values in the plots are normalized so that the $I-V$ and EL image features become comparable across modules and brands.

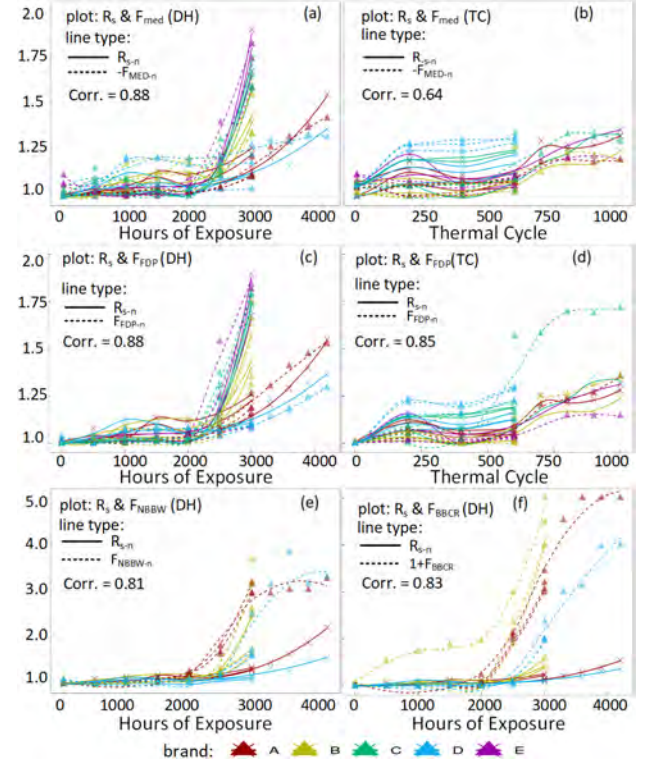


Fig. 8. Plots show trends for normalized series resistance R_{s-n} and the four EL image features extracted from EL images taken stepwise through accelerated exposures. (a) and (b) Plots for R_{s-n} and $-F_{med-n}$ (normalized median intensity of module images) through DH and TC, respectively. (c) and (d) Plots for R_{s-n} and F_{FDP-n} under DH and TC, respectively. (e) and (f) Plots for R_{s-n} and F_{NBBW-n} , and R_{s-n} and F_{BBCR} , respectively, under DH for brands A, B, and D only. Solid lines in all the plots correspond to R_{s-n} , while dashed lines indicate EL image features. Curve fitting in these plots was done with Loess (local regression).

All the subsequent normalized values of features are calculated by dividing the data points by the baseline value (value at 0 hour for DH or 0 cycles for TC) of a module brand.

Fig. 8(a) and (b) shows the time-series of R_{s-n} with $-F_{med-n}$ for all five brands as they are exposed to stressors under DH and TC, respectively. It is also evident from the large value of R_{s-n} and $-F_{med-n}$ in Fig. 8(a) compared with (b) that the modules under DH degrade differently and experience greater power loss when compared with TC exposure condition. We also observe that the correlation value of 0.88 in Fig. 8(a) is much higher than the correlation value in Fig. 8(b), indicating that image darkening in DH is more related to R_{s-n} than in TC. Similarly, plots in Fig. 8(c) and (d) are drawn for EL image feature F_{FDP-n} and R_{s-n} under DH and TC exposures, respectively. Like $-F_{med-n}$, F_{FDP-n} follows the trend of R_{s-n} in each exposure type with high correlation values (0.88 for DH and 0.85 for TC). Fig. 8(e) and (f) shows the time-series trends of F_{NBBW-n} and F_{BBCR} alongside eight for module brands A, B, and D under DH exposure, because of these brands exhibiting busbar darkening in this exposure type. Therefore, to predict the series resistance associated with busbar darkening in EL images, we use F_{NBBW-n} and F_{BBCR} to build two-degree polynomial regression models to predict R_{s-n} .

TABLE I
QUADRATIC POLYNOMIAL MODELS FOR PREDICTING NORMALIZED SERIES RESISTANCE (R_{s-n}) FROM GIVEN EL IMAGE FEATURE X UNDER DH FOR MODULE BRANDS A, B, AND D

$R_{s-n} = \beta_0 + \beta_1 X + \beta_2 X^2$				Adjusted- R^2		RMSE		MAPE	
X	β_0	β_1	β_2	Mean	Std. dev.	Mean	Std. dev.	Mean	Std. dev.
F_{NBBW-n}	1.192	1.992	0.360	0.61	0.057	0.049	0.034	6.88	4.50
F_{BBCR}	1.196	2.119	0.725	0.73	0.025	0.055	0.035	6.82	1.75

The EL image feature for each model is shown in column X and the values of parameters β_0 , β_1 , and β_2 for each model are shown alongside. Mean and standard deviation of model performance metrics from five-fold cross validation are also presented for each model.

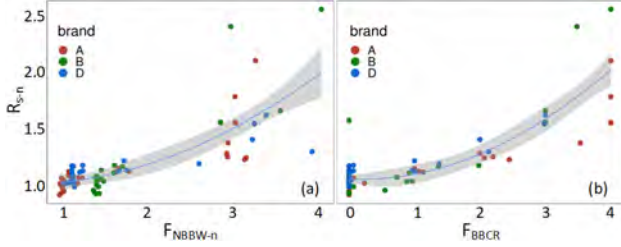


Fig. 9. Normalized series resistance (R_{s-n}) predictive models using F_{NBBW-n} and F_{BBCR} as the independent variables. The gray-shaded region along the regression line is the 95% confidence interval.

In Table I, we show two quadratic polynomial models, and the rows corresponding to F_{NBBW-n} and F_{BBCR} models in the table have their coefficients calculated by using the dataset from brands A, B, and D in DH exposure. The three performance metrics, adjusted- R^2 , root mean square error (RMSE), and mean absolute percentage error (MAPE) are shown in their corresponding rows along with the coefficients of the models. To compare the F_{NBBW-n} and F_{BBCR} , the regression plots of the quadratic models for (R_{s-n}) is shown in Fig. 9.

The mean and standard deviation in Table I are calculated by five-fold cross validation, in which the dataset is split into five folds, a regression model is trained on four folds together, and the adjusted- R^2 , RMSE, and MAPE are calculated on the fifth fold (test dataset). The RMSE value is calculated on original (unnormalized) values after multiplying the normalized values with a normalizing factor. This process is repeated five times by switching one fold of the dataset as a test set and the remaining four-folds as the training set in each iteration.

D. Maximum Power Prediction From EL Image Features

Maximum power (P_{mp}) is a critical value of interest in degradation analysis as this directly relates to the module's performance or energy production. In the heatmap shown in Fig. 7, the correlation coefficients of P_{mp} to F_{med} , and F_{FDP} on full dataset are 0.82, and -0.89 while the correlation of P_{mp} with F_{NBBW} , and F_{BBCR} for brand A, B, and D under DH is -0.76 and -0.86 , respectively. Similar to Fig. 8, which shows the trends of R_{s-n} and EL image features, Fig. 10 shows the time-series of normalized P_{mp} (P_{mp-n}) with normalized EL image features. Fig. 10(e) and (f) uses data from brands A, B, and D through DH exposure, whereas remaining plots (a–d) use all module brands through both DH and TC exposure types. In all plots of Fig. 10,

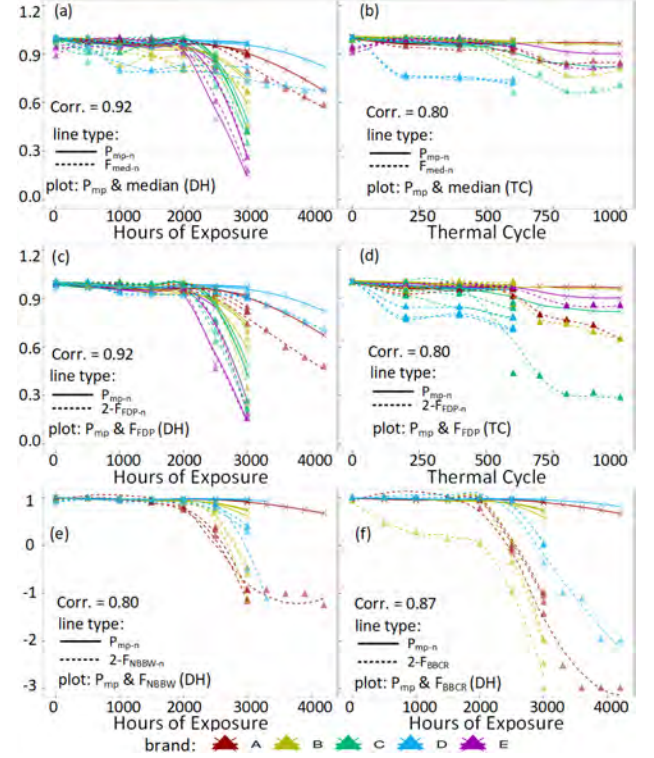


Fig. 10. Plots show time-series of normalized P_{mp} (P_{mp-n}) and four module-level EL image features through accelerated exposures. (a) and (b) Plots for P_{mp-n} and F_{med-n} (normalized median intensity of module images) under DH condition and TC, respectively. (c) and (d) Plots for P_{mp-n} and $1 - F_{FDP-n}$ under DH and TC, respectively. (e) and (f) Plots for P_{mp-n} and $1 - F_{NBBW-n}$, and P_{mp-n} and $1 - F_{BBCR}$, respectively, for DH exposure of brands A, B, and D. Solid lines in all the plots are for P_{mp-n} and the dashed lines are for the corresponding EL image feature. Correlation values between P_{mp-n} and EL image features are shown in each plot. Curve fitting in these plots are done using local regression.

we observe that EL image features are highly correlated with P_{mp-n} , and, thus, they can serve as predictors for P_{mp-n} .

The coefficients of the predictive models and their performance metrics for normalized P_{mp} (P_{mp-n}) from four EL features are shown in Table II and the regression plots of the models are shown in Fig. 11. Mean and standard deviation of the performance metrics (adjusted- R^2 , RMSE, and MAPE) are calculated using five-fold cross validation. The regression models shown in Fig. 11(a) and (b) uses F_{med-n} and F_{FDP-n} variables, respectively, to predict P_{mp-n} for all brands in both TC and DH exposures, whereas Fig. 11(c) and (d) shows predictive models for P_{mp-n} with independent variables F_{NBBW-n} and

TABLE II
THIRD DEGREE POLYNOMIAL MODELS FOR PREDICTING NORMALIZED MAXIMUM POWER (P_{mp-n}) FROM GIVEN EL IMAGE FEATURE X FOR ALL MODULES IN DH AND TC

$P_{mp-n} = \beta_0 + \beta_1 X + \beta_2 X^2 + \beta_3 X^3$					Adjusted- R^2		RMSE		MAPE	
X	β_0	β_1	β_2	β_3	Mean	Std. dev.	Mean	Std. dev.	Mean	Std. dev.
$1 - F_{med-n}$	0.936	-1.396	-0.756	-0.039	0.88	0.025	11.87	5.57	3.46	1.58
F_{FDP-n}	0.936	-1.502	-0.478	-0.128	0.87	0.016	12.44	4.96	3.94	2.08
F_{NBBW-n}	0.935	-0.576	-0.064	-0.005	0.70	0.03	13.35	10.53	4.34	3.08
F_{BCCR}	0.932	-0.650	-0.204	0.014	0.81	0.017	9.53	4.75	2.83	1.45

The EL image feature for each model is shown in column X and the values of parameters $\beta_0, \beta_1, \beta_2, \beta_3$ for each model are shown alongside. Mean and standard deviation of model performance metrics from five-fold cross validation are also presented for each model.

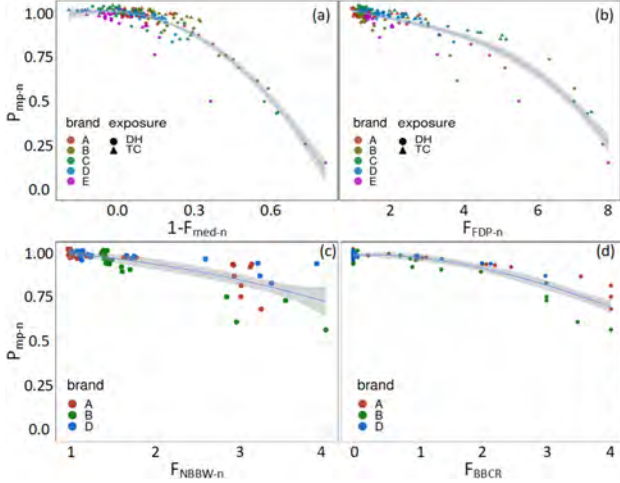


Fig. 11. Normalized power P_{mp-n} predictive model using four normalized EL features: (a) $1 - F_{med-n}$, (b) F_{FDP-n} , (c) F_{NBBW-n} , and (d) F_{BCCR} . The gray-shaded region along the regression line is the 95% confidence interval.

F_{BCCR} , respectively, for only brands A, B, and D under DH exposure.

V. DISCUSSION

The recent works in automated detection of various cell degradation types [12], [35], [36] leveraged EL images and machine learning methods. We demonstrate in Fig. 7 that the $I-V$ features P_{mp} and R_s have high Pearson correlation coefficients with four EL image features F_{med} , F_{FDP} , F_{NBBW} , and F_{BCCR} . Some stratification can be seen in F_{FDP} pairs plots because of different brand or exposure type, but as shown brand- and exposure-wise in Fig. 11, it is not conclusive enough to warrant a multilevel modeling approach. Pairs plots for F_{NBBW} show two clusters as a result of the change-point degradation behavior of PV modules in accelerated exposures; modules usually degrade slowly for up to 2500 h (Figs. 8 and 10) and, then, exhibit rapid degradation thereafter. F_{BCCR} has distinct levels because of the quantized classification of cell busbar corrosion (see Fig. 4). This work applies automated feature extraction from EL images of PV modules in two ways: 1) quantification of mechanistic R_s degradation, and 2) generalized prediction of module power.

1) *Feature-Based Quantification of Mechanistic Degradation:* Mechanism-specific prediction of PV module electrical performance from EL image features is important for rapid identification and quantification of module defects in manufacturing,

TABLE III
CONFUSION MATRIX FOR CNN MODEL CELL CLASSIFICATION INTO FIVE CORROSION LEVELS IN ORDER OF INCREASING SEVERITY FROM 0 TO 4 AS SHOWN IN FIG. 4

		Predicted class					Recall
		0	1	2	3	4	
Actual class	0	527	8	0	0	0	0.98
	1	20	112	5	0	0	0.81
	2	0	4	82	3	0	0.92
	3	0	0	2	62	2	0.93
	4	0	0	0	2	60	0.96
Precision		0.96	0.90	0.92	0.92	0.96	

Precision and recall metrics for each class are represented by last row and last column, respectively.

as well as degradation in power plant operations and management. In PV research, this capability combined with statistically significant module EL image data and knowledge of modules' bill of materials can help to identify cell types, materials, and fielding conditions that lead to specific degradation modes in PV modules. Toward this goal, we first demonstrated methods to calculate two EL image features (F_{NBBW} and F_{BCCR}) that quantify a specific degradation feature: the width of busbar darkening.

As only three brands (A, B, and D) under DH exhibit busbar darkening, we used data only from these modules to model series resistance from EL image features.

All four EL features have high correlation among themselves (see Fig. 7), it is because they quantify the darkening of EL images in various ways. Despite all EL features having high correlation between them, they represent different aspects of cell degradation. F_{med} represents overall health of PV module, F_{FDP} represents the fraction of the surface area of PV module that is functioning poorly, F_{NBBW} gives the normalized value of busbar width independent of the number of busbars, and F_{BCCR} uses cell classification by busbar corrosion level and averages for a module-level value. It is important to emphasize, we have only used F_{NBBW} , and F_{BCCR} features to predict R_{s-n} because an increase in busbar corrosion leads to high R_s [37].

For F_{NBBW} , we directly calculate the width of the darkened busbar region from cell images (shown in Fig. 3 and Equation 1), whereas for F_{BCCR} , we first classify the cells into either of the five classes based on the severity level of corrosion (using CNN model in Fig. 5) and calculate the average corrosion level for all cells in the module to obtain F_{BCCR} .

The CNN models used to predict the classes of cell (see Table III) classified the cells with high accuracy of over 94%. In addition, we observe in Fig. 7 that F_{BCCR} and F_{NBBW} have

a high correlation of 0.92, which confirms that F_{BCCR} derived from supervised machine learning classification is a good representation of busbar corrosion width F_{NBBW} , while being more adaptable to new data. In using EL image features to predict series resistance of modules, Table I shows that the F_{BCCR} model has the better adjusted- R^2 (0.73) of the two mechanistic EL image features for predicting R_{s-n} . Furthermore, the 95% confidence interval (shaded region) in Fig. 9 of the F_{BCCR} model is narrower compared with F_{NBBW} model.

2) *Generalized Power Prediction*: Generalized module power prediction is critical for large-scale PV plants where operation and management is not feasible by traditional methods of manual screening of PV modules. In this article, we demonstrated the correlation of PV module's P_{mp} and EL features, which are F_{med} , F_{FDP} , F_{NBBW} , and F_{BCCR} (see Fig. 10). We build generalized power prediction models using data from five PV module brands under two different exposure types to predict normalized P_{mp} from intensity-based EL image features $F_{\text{med}-n}$, or $F_{\text{FDP}-n}$ (shown in Fig. 11(a) and (b), and Table II). Since the decrease in pixel intensity of EL images is proportional to power loss in the PV device, features that directly measure the proportion of dark regions in an image gives better prediction of P_{mp} results than the features that measure one mechanistic degradation, i.e., width of busbar corrosion. This is evident from the models in Table II, $F_{\text{med}-n}$, and $F_{\text{FDP}-n}$ have high adjusted- R^2 (0.88 and 0.87) and similar error values for RMSE (11.87 and 12.44) and MAPE (3.46 and 2.83) when compared with $F_{\text{NBBW}-n}$ and F_{BCCR} , which are only calculated for brands A, B, and D under DH exposure. Hence, the more generalized intensity-based EL image features account for all power loss mechanisms present in the cells, whereas mechanistic-specific features such as $F_{\text{NBBW}-n}$ and F_{BCCR} are not effective for generalized power prediction. Therefore, our module power predictive models using the module EL image intensity-based features $F_{\text{med}-n}$ and $F_{\text{FDP}-n}$ are independent of cell type and degradation mode.

Because of the high quality of modern PV modules and the nature of their response to DH and TC accelerated exposures, most data points used to build the predictive models in Figs. 9 and 11 are clustered toward low degradation (high power/low series resistance). The 95% confidence interval demonstrate model response to data variance.

The predictive models discussed above were built using $I-V$ and EL image features normalized to initial (pre-exposure) values. This way, we were able to accurately predict module power and series resistance changes across brands and Si cell technologies with generalized models. In the real world, using this method to predict degraded module electrical performance from EL images would require initial characterization of the module at the time of fielding. This practice is realistic with recent advances in high-speed PV module imaging technologies for the field survey, and is highly desired by investors and power plant owners to validate and demonstrate the quality and capacity of new installations. Furthermore, PV module in-line characterization at the time of manufacture is now ubiquitous, so vertically integrated PV companies already possess initial module data required for normalization.

VI. CONCLUSION

In this article, we developed models to predict PV module $I-V$ features from EL image characteristics. Generalized predictive models using robust EL image intensity-based features including median pixel intensity (F_{med}) and the fraction of dark pixels (F_{FDP}) demonstrated high P_{mp} prediction accuracy for 195 EL and $I-V$ measurements of 30 PV modules spanning five brands and three cell types in two accelerated exposures. F_{med} and F_{FDP} generalized predictive models of P_{mp} had high adjusted- R^2 values of 0.88 and 0.87, respectively. We also demonstrated EL image feature quantification of mechanistic degradation, using both pixel-based and supervised machine learning classification approaches to measure busbar darkening in cell-level EL images. The module-level features derived from cell-level quantities, F_{NBBW} and F_{BCCR} , were then used to build predictive models for module series resistance (R_s). Of the two models, the model based on the supervised machine learning classification feature (F_{BCCR}) exhibited the higher adjusted- R^2 of 0.73 and more narrow band for 95% confidence interval. The CNN model used to derive F_{BCCR} classified cell-level images based on severity of busbar darkening with high accuracy of over 94%. These performance predictive methods require only initial characterization of a PV module with EL imaging and $I-V$ curve tracing, and can, then, be used to estimate the modules power output at any time up to module failure from the EL image of the degraded module. This enables high-speed *in-situ* power estimation for fielded PV modules, and a framework for understanding large-scale mechanistic degradation of PV modules at high resolution. Additionally, these methods can be applied across the manufacturing, operations and management, and research and development facets of the PV community to enhance the speed, quality, and usefulness of cell- and module-level image-based characterization.

ACKNOWLEDGMENT

This work made use of the High Performance Computing Resource in the Core Facility for Advanced Research Computing at Case Western Reserve University.

REFERENCES

- [1] M. Köntges *et al.*, "Review of failures of photovoltaic modules," Tech. Rep. IEA-PVPS T13-01:2014, Photovoltaic Power Systems Programme, Int. Energy Agency, Paris, France, 2014.
- [2] T. J. Peshek *et al.*, "Insights into metastability of photovoltaic materials at the mesoscale through massive I-V analytics," *J. Vacuum Sci. Technol. B*, vol. 34, no. 5, Sep. 2016, Art. no. 050801.
- [3] D. C. Jordan, T. J. Silverman, J. H. Wohlgemuth, S. R. Kurtz, and K. T. VanSant, "Photovoltaic failure and degradation modes," *Prog. Photovolt.: Res. Appl.*, vol. 25, no. 4, pp. 318–326, Apr. 2017.
- [4] R. H. French *et al.*, "Degradation science: Mesoscopic evolution and temporal analytics of photovoltaic energy materials," *Current Opinion Solid State Mater. Sci.*, vol. 19, no. 4, pp. 212–226, Aug. 2015.
- [5] T. M. Pletzer, J. I. van Mölken, S. Rißl and, O. Breitenstein, and J. Knoch, "Influence of cracks on the local current-voltage parameters of silicon solar cells," *Prog. Photovolt.: Res. Appl.*, vol. 23, no. 4, pp. 428–436, Apr. 2015.
- [6] J. S. Fada *et al.*, "Democratizing an electroluminescence imaging apparatus and analytics project for widespread data acquisition in photovoltaic materials," *Rev. Scientific Instrum.*, vol. 87, no. 8, Aug. 2016, Art. no. 085109.

- [7] T. Trupke, J. Nyhus, and J. Haunschild, "Luminescence imaging for inline characterisation in silicon photovoltaics," *Physica Status Solidi (RRL)-Rapid Res. Lett.*, vol. 5, no. 4, pp. 131–137, 2011.
- [8] D. Hinken, K. Ramspeck, K. Bothe, B. Fischer, and R. Brendel, "Series resistance imaging of solar cells by voltage dependent electroluminescence," *Appl. Phys. Lett.*, vol. 91, no. 18, 2007, Art. no. 182104.
- [9] J. S. Fada *et al.*, "Electroluminescent image processing and cell degradation type classification via computer vision and statistical learning methodologies," in *Proc. IEEE 44th Photovolt. Spec. Conf.*, Jun. 2017, pp. 3456–3461.
- [10] J. S. Fada *et al.*, "Correlation of I-V curve parameters with module-level electroluminescent image data over 3000 hours damp-heat exposure," in *Proc. IEEE 44th Photovolt. Spec. Conf.*, Washington, D.C., USA, Jun. 2017, pp. 2697–2701.
- [11] A. M. Karimi *et al.*, "Feature extraction, supervised and unsupervised machine learning classification of PV cell electroluminescence images," in *Proc. IEEE 7th World Conf. Photovolt. Energy (A Joint Conf. 45th IEEE PVSC, 28th PVSEC 34th EU PVSEC)*, Jun. 2018, pp. 0418–0424.
- [12] A. M. Karimi *et al.*, "Automated pipeline for photovoltaic module electroluminescence image processing and degradation feature classification," *IEEE J. Photovolt.*, vol. 9, no. 5, pp. 1324–1335, Sep. 2019.
- [13] X. Ma *et al.*, "Data-driven I-V feature extraction for photovoltaic modules," *IEEE J. Photovolt.*, vol. 9, no. 5, pp. 1405–1412, Sep. 2019.
- [14] K. Ramspeck *et al.*, "Recombination current and series resistance imaging of solar cells by combined luminescence and lock-in thermography," *Appl. Phys. Lett.*, vol. 90, no. 15, 2007, Art. no. 153502.
- [15] T. Potthoff, K. Bothe, U. Eitner, D. Hinken, and M. Koentges, "Detection of the voltage distribution in photovoltaic modules by electroluminescence imaging," *Prog. Photovolt.: Res. Appl.*, vol. 18, no. 2, pp. 100–106, Mar. 2010.
- [16] S. Deitsch, C. Buerhop-Lutz, A. Maier, F. Gallwitz, and C. Riess, "Segmentation of photovoltaic module cells in electroluminescence images," Jun. 2018, *arXiv:1806.06530*.
- [17] T. Fuyuki, H. Kondo, T. Yamazaki, Y. Takahashi, and Y. Uraoka, "Photographic surveying of minority carrier diffusion length in polycrystalline silicon solar cells by electroluminescence," *Appl. Phys. Lett.*, vol. 86, no. 26, Jun. 2005, Art. no. 262108.
- [18] T. Fuyuki, H. Kondo, Y. Kaji, A. Ogane, and Y. Takahashi, "Analytic findings in the electroluminescence characterization of crystalline silicon solar cells," *J. Appl. Phys.*, vol. 101, no. 2, Jan. 2007, Art. no. 023711.
- [19] T. Fuyuki and A. Kitiyanan, "Photographic diagnosis of crystalline silicon solar cells utilizing electroluminescence," *Appl. Phys. A*, vol. 96, no. 1, pp. 189–196, Jul. 2009.
- [20] *Terrestrial photovoltaic (PV) modules - Design qualification and type approval - Part 2: Test procedures*, International Electrotechnical Commission, International Standard, IEC 61215-2:2016, 2016.
- [21] "coolSamBa HR-830 cooled scientific camera - for electroluminescence," 2019.
- [22] R. French, A. Karimi, and J. Braid, "EL-cell-images-single-brand-dampheat," Dec. 2019, doi: [10.17605/OSF.IO/8ZKQG](https://doi.org/10.17605/OSF.IO/8ZKQG).
- [23] A. M. Karimi *et al.*, "PVMage: Package for PV image analysis and machine learning modeling," *Version 0.0.4*, Feb. 2020.
- [24] J. S. Fada, "Modeling degradation of photovoltaic modules using machine learning of electroluminescent images," Ph.D. dissertation, Dept. Higher Edu., Case Western Reserve Univ., Cleveland, OH, USA, 2018.
- [25] A. Krizhevsky, I. Sutskever, and G. E. Hinton, "ImageNet classification with deep convolutional neural networks," in *Proc. Adv. Neural Inf. Process. Syst.*, 2012, pp. 1097–1105.
- [26] P. Simard, D. Steinkraus, and J. Platt, "Best practices for convolutional neural networks applied to visual document analysis," in *Proc. 7th Int. Conf. Document Anal. Recog.*, 2003, vol. 1, pp. 958–963.
- [27] S. Lawrence, C. L. Giles, A. C. Tsoi, and A. D. Back, "Face recognition: A convolutional neural-network approach," *IEEE Trans. Neural Netw.*, vol. 8, no. 1, pp. 98–113, Jan. 1997.
- [28] M. Egmont-Petersen, D. de Ridder, and H. Handels, "Image processing with neural networks—A review," *Pattern Recognit.*, vol. 35, no. 10, pp. 2279–2301, Oct. 2002.
- [29] W. Liu *et al.*, "A survey of deep neural network architectures and their applications," *Neurocomputing*, vol. 234, pp. 11–26, Apr. 2017.
- [30] M. Abadi *et al.*, "TensorFlow: A system for large-scale machine learning," in *Proc. 12th USENIX Symp. Operating Syst. Des. Implementation*, 2016, pp. 265–283.
- [31] F. Chollet *et al.*, *Keras*, 2015. [Online]. Available: <https://keras.io>
- [32] Python Core Team, "Python 3.6.9," Python: A dynamic, open source programming language, Python Software Foundation, 2019. [Online]. Available: <https://www.python.org/>
- [33] E. Garcia, "A tutorial on correlation coefficients," in *Semantic Scholar*. Semantic Scholar, 2011, p. 13.
- [34] W. G. Jacoby, "Loess: A nonparametric, graphical tool for depicting relationships between variables," *Electoral Studies*, vol. 19, no. 4, pp. 577–613, 2000.
- [35] M. Alt *et al.*, "Electroluminescence imaging and automatic cell classification in mass production of silicon solar cells," in *Proc. 7th World Conf. Photovolt. Energy Convers. (Joint Conf. 45th IEEE PVSC, 28th PVSEC, 34th EU PVSEC)*, 2018, pp. 3298–3304.
- [36] S. Deitsch *et al.*, "Automatic classification of defective photovoltaic module cells in electroluminescence images," *Sol. Energy*, vol. 185, pp. 455–468, Jul. 2018.
- [37] R. Asadpour, X. Sun, and M. A. Alam, "Electrical signatures of corrosion and solder bond failure in c-Si solar cells and modules," *IEEE J. Photovolt.*, vol. 9, no. 3, pp. 759–767, May 2019.



Ahmad Maroof Karimi received the B.S. degree in electrical engineering from Aligarh Muslim University, Aligarh, India, in 2011. He received the M.S. degree in computer science from the University of Toledo, Toledo, OH, USA, in 2016. He is currently working toward the Ph.D. degree in computer science from Case Western Reserve University (CWRU), Cleveland, OH, USA.



He joined the Solar Durability Lifetime Extension Research Center, CWRU, in 2017 as a Research Assistant. His research work includes the application of computer vision, machine learning, pattern recognition, and data mining in the field of energy applications. His interests also include working on large-scale distributed computing clusters for real-time machine learning problems.

Justin S. Fada received the B.S. degree with dual majors in mechanical and aerospace engineering in 2017 and the M.S. degree in mechanical engineering from Case Western Reserve University, Cleveland, OH, USA, in 2018.

He is currently working with the National Aeronautics and Space Administration as an Aerospace Engineer. He joined the Solar Durability and Lifetime Extension Research Center in 2014 as an Undergraduate Researcher working on various projects related to the degradation of devices and materials subject to natural and induced environments. He developed imaging systems and analytic methods for understanding how PV devices degrade.



Nicholas A. Parrilla received the B.S. degree in physics with a concentration in mathematical physics from Case Western Reserve University, Cleveland, OH, USA, in 2019.

Following graduation, he worked as a Materials Engineer with Folio Photonics, Solon, OH, USA, before seeking to expand his industry and research experience in Ithaca, NY, USA. He had researched optimization techniques with applications to nuclear fusion with Cornell University and currently works as an Electronics Engineer in Syracuse, NY, USA.

He joined the Solar Durability and Lifetime Extension Research Center in 2016, initially working on predictive modeling of PV power plant performance before working on image analysis software for PV applications.



Benjamin G. Pierce is currently working toward the integrated B.S./M.S. degree in computer science with Case Western Reserve University, Cleveland, OH, USA.

In Fall 2018, he joined the Solar Durability and Lifetime Extension Research Group as an Undergraduate Researcher. He is currently working on image analysis of electroluminescence images of photovoltaic modules. His research interests include data science for other materials, machine learning, and computer vision.



Mehmet Koyuturk received the B.S. and M.S. degrees from Bilkent University, Ankara, Turkey, respectively, in electrical engineering and computer engineering, and the Ph.D. degree in computer science from Purdue University, West Lafayette, IN, USA, in 2006.

He is the Andrew R. Jennings Professor of computing sciences with the Department of Computer and Data Sciences, Case Western Reserve University, Cleveland, OH, USA. His research interests include the development of algorithms for large-scale data mining and analysis, with particular emphasis on networks and graph-structured data. He particularly focuses on biology and energy as application areas, and develops algorithms for analyzing biological networks and gaining insights into the systems biology of complex diseases.

Dr. Koyuturk is an Associate Editor for IEEE/ACM TRANSACTIONS ON COMPUTATIONAL BIOLOGY AND BIOINFORMATICS.



Jennifer L. Braid (Member, IEEE) received the B.S. degree in physics and mathematics from Ohio University, and the M.S. degree in physics from the Ohio State University, Columbus, OH, USA, and the Ph.D. degree in applied physics from Colorado School of Mines, Golden, CO, USA, in 2016, while conducting research in organic photovoltaics with the National Renewable Energy Laboratory.

She is a Research Assistant Professor with Case Western Reserve University, Cleveland, OH, USA, and currently a Visiting Researcher with Sandia National Laboratories, Albuquerque, NM, USA. In addition to image processing and computer vision, her current research interests include data mining and dimension reduction techniques for performance and degradation analysis of laboratory and field PV data.

Dr. Braid received the EERE Postdoctoral Research Award in 2019 to develop image processing methods for laboratory and field imaging techniques for PV modules.



Roger H. French (Member, IEEE) received the Ph.D. degree in materials science from Massachusetts Institute of Technology, Cambridge, MA, USA, under Professor R. L. Coble.

He was with DuPont Company, Central Research from 1985 and was Adjunct Professor of materials science with the University of Pennsylvania in 1996. He has been the Kyocera Professor with the Department of Materials Science with secondary appointments in macromolecular science, computer and data sciences, biomedical engineering and physics, Case Western Reserve University, Cleveland, OH, USA, since August 2010. He is the Director of the SDLE Research Center, and the Faculty Director of the CWRU Applied Data Science Program. His research interests include lifetime and degradation science, and reliability, of photovoltaic materials, modules, and power plants, using data science and high-performance/distributed computing approaches.